Volume 13
Number 23
21 June 2025
Pages 17137–18016

Journal of Materials Chemistry A

Materials for energy and sustainability

rsc.li/materials-a

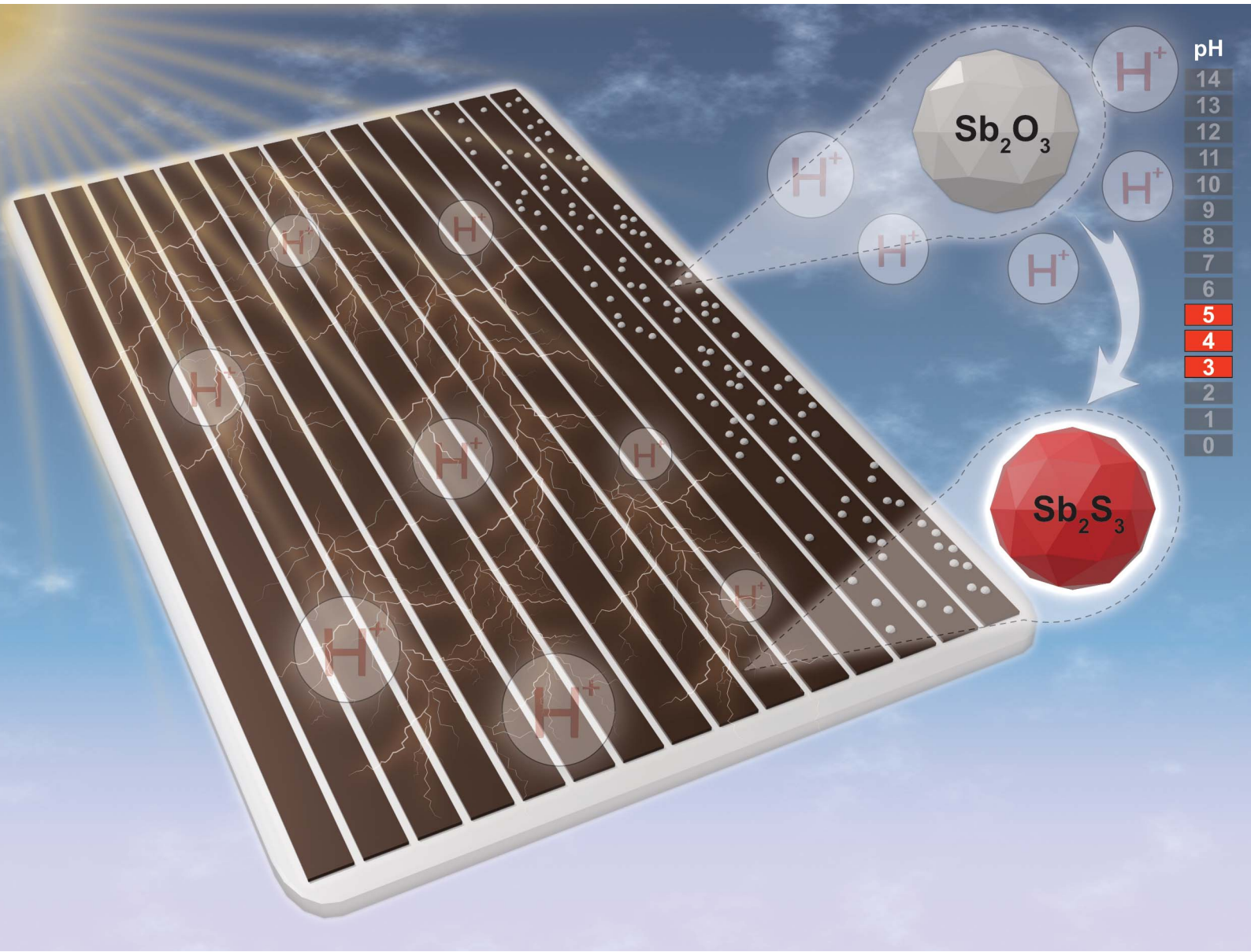

ISSN 2050-7488

ROYAL SOCIETY OF CHEMISTRY

PAPER

Tayebeh Ameri *et al.*

Establishing design principles for functional additives in antimony chalcogenide solar cells

Journal of Materials Chemistry A

ROYAL SOCIETY OF CHEMISTRY

PAPER

View Article Online
View Journal | View Issue

Cite this: J. Mater. Chem. A, 2025, 13, 17340

Establishing design principles for functional additives in antimony chalcogenide solar cells†

Matthew Sutton, [a] Neil Robertson [b] and Tayebeh Ameri *[acd]

Received 5th February 2025
Accepted 25th March 2025

DOI: 10.1039/d5ta00947b

rsc.li/materials-a

Antimony chalcogenide solar cells are a promising thin-film solar technology, offering a tunable bandgap, high intrinsic stability, and a large absorption coefficient. Their solution-processability enables the straightforward incorporation of chemical additives. While many additives have been explored, their underlying chemical mechanisms remain poorly understood. In this study, we examine the chemical mechanism of a proven additive, EDTA, and leverage these insights to develop a screening process for identifying additives that match or surpass its performance. Our findings reveal a dual role of EDTA and similar molecules: (i) Sb^{3+} chelation, enhancing Sb_2S_3 film quality, and (ii) pH reduction in the precursor solution, suppressing Sb_2O_3 formation. Additionally, we propose a chemical mechanism for the *in situ* conversion of Sb_2O_3 to Sb_2S_3. These insights will aid in the rational design of future additives and establish general guidelines for optimizing the growth conditions of efficient antimony chalcogenide solar absorbers under widely used hydrothermal conditions.

1 Introduction

As a result of the increasing effects of climate change, renewable sources of energy such as solar energy are growing in importance. Solar power generation has been accelerating in recent years, with global generation reaching 4264 TW h (2.33% of total) in 2022, up from 3446 TW h (1.92% of total) the previous year.[1,2] Silicon solar cells currently dominate the market. However, there is scope for lightweight solar technologies for use on electric vehicles.

Antimony chalcogenides (Sb_2E_3, E = S,Se) are non-toxic,[3–10] highly stable *vs.* moisture and air,[3,6,7,11,12] have a strong absorption coefficient of $>10^5$ cm^{-1} at visible wavelengths[3–11] and are comprised of earth-abundant materials.[3–10] Sb_2E_3 has a variety of processing techniques, and is annealed at relatively low temperature (<400 °C).[3–6,11–23] Additionally, the S sites in Sb_2S_3 can be interchanged for Se without changing the stibnite crystal structure to form Sb_2E_3, so the band gap can be adjusted between 1.1–1.8 eV and so be optimised for solar cell applications.[3–7,11,12,24] Sb_2E_3 is a thin-film technology, allowing the absorber layer thickness to be optimised at around 300 nm,[3,13,16,20,25] compared with the optimum for monocrystalline silicon of 170 μm.[26] This represents an approximate 500-fold reduction in optimized thickness for Sb_2E_3, paving the way for decreased material usage and lighter modules compared to traditional silicon.

The main limitation facing antimony chalcogenide solar cells currently is that of low efficiency. To date, the highest efficiency that has been achieved is 10.75%.[22] That record, along with the two previous record efficiencies of 10.7% and 10.5% were achieved through the application of chemical additives *via* hydrothermal deposition.[17,18] Additionally, other additive strategies have been employed, such as the codoping of Sb_2S_3 with Cl and Se by Chen *et al.* (2022), which increased efficiency from 5.9% to 7.15% by reducing bulk and interface defect density.[27] Similarly, Che *et al.* (2025) reported the post-treatment of Sb_2Se_3 with P_2O_5, which suppressed surface defects and minimized gaps between Sb_2Se_3 ribbons.[28] In addition to the improvement of film quality and passivation of crystalline defects, the suppression of unwanted side-phases such as Sb_2O_3 is important to yield high efficiency, and additives such as phosphotungstic acid have previously been used for this purpose.[19,20,29,30] Thus, the study of chemical additives is of great importance in the pursuit of increasing the efficiency of antimony chalcogenide solar cells.

While the material quality and cell efficiency outcomes of these additives have been observed, a deep understanding of their underlying mechanisms remains to be achieved. For example, the record efficiency of 10.75% was achieved by using ethanol as a co-solvent.[22] The hypothesis was that ethanol reduces the solubility of Sb^{3+} in solution, and thus slows down

[a]Institute for Materials and Processes, School of Engineering, University of Edinburgh, Sanderson Building, Robert Stevenson Road, Edinburgh EH9 3FB, UK
[b]School of Chemistry, The University of Edinburgh, David Brewster Road, Edinburgh EH9 3FJ, UK
[c]Chair for Composite Materials, Department of Materials Science, Faculty of Engineering, Christian-Albrechts-Universität zu Kiel, Kaiserstrasse 2, 24143 Kiel, Germany. E-mail: tam@tf.uni-kiel.de
[d]Kiel Nano, Surface and Interface Science KiNSIS, Kiel University, Christian-Albrechts-Platz 4, D-24118 Kiel, Germany

† Electronic supplementary information (ESI) available. See DOI: https://doi.org/10.1039/d5ta00947b

deposition, forming larger grains. Similarly, when EDTA was used to achieve 10.5% efficiency,[17] it was concluded that the EDTA chelates Sb^{3+} and preferentially deposits it on the film, leading to a faster ion-based deposition rather than a nanoparticle-based deposition, leading to large and compact grains. While ethanol was shown to directly reduce the solubility of the precursor potassium antimony tartrate, the evidence for the effectiveness of EDTA was only given in the form of improved film quality and/or altered deposition rate. Thus, direct chemical evidence of the proposed mechanisms of EDTA was not provided. We believe that in-depth fundamental studies of such mechanisms are essential to deepen current understanding. As such, we chose to conduct a deeper investigation into the effects of EDTA, and to probe its interactions with the hydrothermal precursors in order to elucidate how it improves film quality and cell efficiency.

2 Results and discussion

2.1 EDTA in Sb_2S_3/TiO_2 solar cells

Before investigating the mechanisms of EDTA, we first confirmed its effectiveness as an additive in the Sb_2S_3/TiO_2 system, which we selected over $Sb_2(S,Se)_3$/CdS for safety and environmental reasons detailed in ESI Discussion 1.† We used the precursors potassium antimony tartrate (PAT) and sodium thiosulfate (STS). We fabricated cells using EDTA, and achieved efficiency gains similar to those seen by Wang *et al.*,[17] with an increase from 2.88 to 4.14 (1.26%) in our case, compared to the increase from 9.4 to 10.5% (1.1%) for Wang *et al.* using the $Sb_2(S,Se)_3$/CdS system. The *J*–*V* and EQE curves of the champion cells are shown in Fig. 1. Cell statistics are shown in ESI Fig. 1 and Table 2.† The enhanced performance following the addition of EDTA demonstrates its effectiveness as an additive in Sb_2S_3/TiO_2 solar cells.

In the original study on EDTA, the performance improvement was largely attributed to higher film quality. Therefore, we looked at the surface of our bare Sb_2S_3/TiO_2 films to confirm if this was the case for our cells too. Fig. 2 shows the surfaces of the standard (additive-free) and the EDTA Sb_2S_3 films under scanning electron microscopy (SEM). The surface of the standard film is covered with unevenly shaped formations, while the surface of the EDTA film is even and smooth. The crystals were proven to be Sb_2O_3 by powder X-ray diffraction (p-XRD), Raman mapping and SEM-EDS (ESI Fig. 2–4†). Sb_2O_3 is an insulator and known unwanted impurity in antimony chalcogenide solar cells,[19,20,29,30] so it likely contributed to the standard film's poorer performance.

The improvements made in Sb_2S_3 crystallinity by EDTA in literature were mainly in terms of increased grain size, with some marginal improvement in orientation, shown by the texture coefficient (TC) of the films.[17] Since antimony chalcogenides are a 1-D material, charge transport is favoured along the 'ribbons' and therefore, an *hkl*-orientated film (with the ribbons running between the transport layers) yields favourable performance. In our case, $TC_{(211)}$ increased from 0.37 for the standard to 0.43 for EDTA, as did $TC_{(221)}$ from 0.30 to 0.37 (calculation given in ESI eqn (1)).† The ratio $TC_{(211)}/TC_{(120)}$ also increased from 0.45 to 0.51 from the standard to EDTA. Each of these changes replicated those seen in literature.[17] Grain size could not be precisely measured due to the presence of Sb_2O_3 formations on the surface of the standard film, so we cannot confirm whether this was a factor in our case. Overall, our results align with those of Wang *et al.*[17] for the $Sb_2(S,Se)_3$ system, with the notable addition of Sb_2O_3 suppression as a key component of EDTA's working mechanism.

2.2 Mechanistic investigation of EDTA

The initially proposed working mechanism of EDTA was hypothesised as "a strong ligand to coordinate Sb^{3+} ions […] able to suppress the formation of $[Sb_2(S,Se)_3]$ precipitate".[17] This $[Sb_2(S,Se)_3]$ precipitate was considered unwanted due to its formation in a particle deposition regime on the bulk film, as

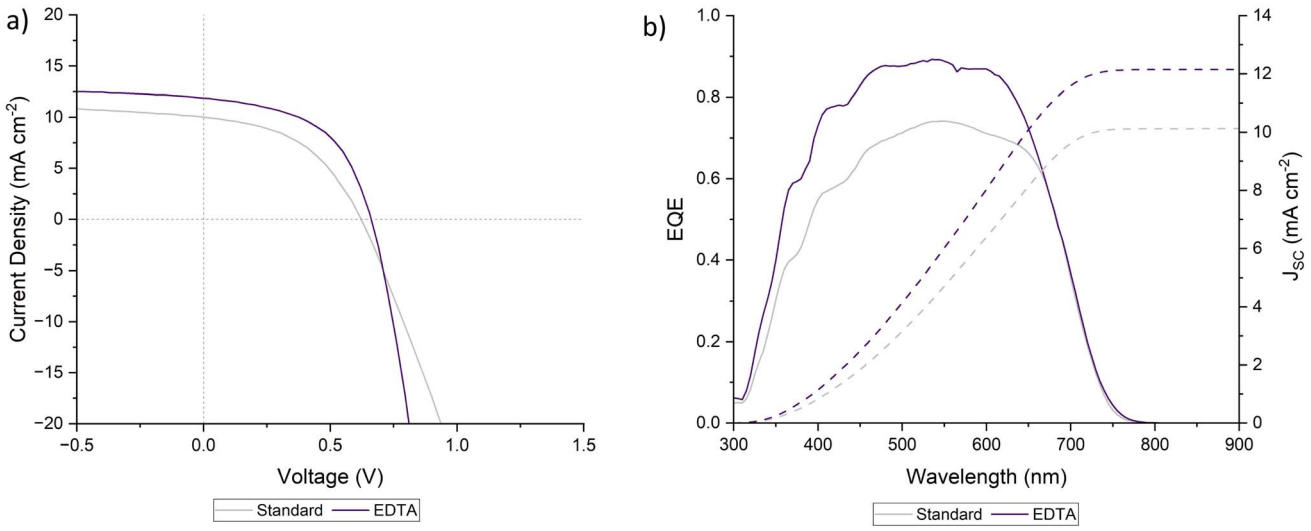

Fig. 1 (a) *J*–*V* curves, and (b) EQE response of champion standard (additive-free) and EDTA Sb_2S_3 solar cells.

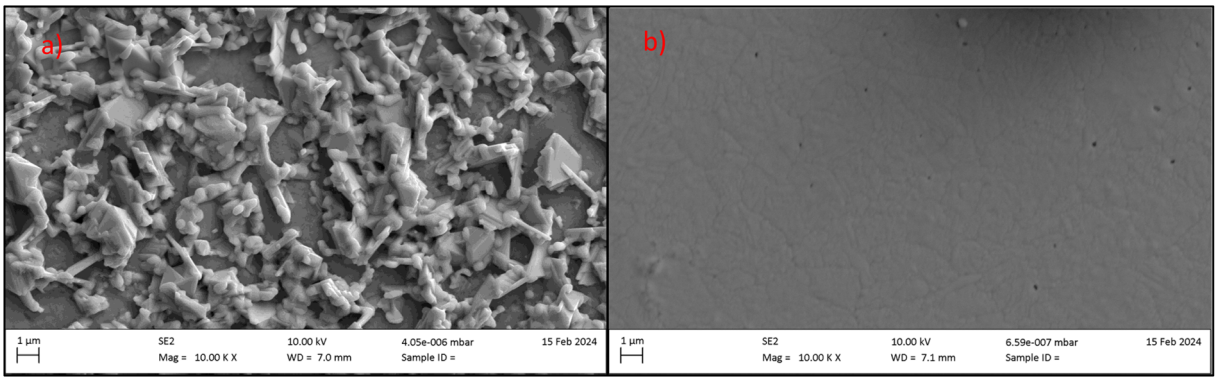

Fig. 2 Sb_2S_3 film quality shown through SEM images of Sb_2S_3 films using (a) no additive and (b) EDTA.

opposed to an ion-reactive regime. A particle deposition regime involves the spontaneous formation of Sb_2S_3 nanoparticles in solution, which then deposit onto the film. In an ion-reactive regime, individual ions deposit onto the film directly, forming Sb_2S_3 as they deposit. An ion reactive regime is thought to result in a more compact film with larger grains. Therefore, we proposed two procedures to test these claims: (i) the binding of EDTA to Sb^{3+} investigated using NMR spectroscopy; (ii) the formation of antimony chalcogenide aggregate in a precursor solution both with and without EDTA, measured over time.

Firstly, NMR spectroscopy was performed on four solutions containing different mixtures of the precursors and EDTA. The resulting spectra are shown in Fig. 3.

EDTA in D_2O is known to produce two clear peaks[31] which correspond to the 'arm' CH_2 groups, which we observed at $\delta =$ 3.94 ppm, and 'backbone' CH_2 groups, which we observed at $\delta =$ 3.62 ppm. When PAT is added to EDTA in D_2O, the arm C-H_2

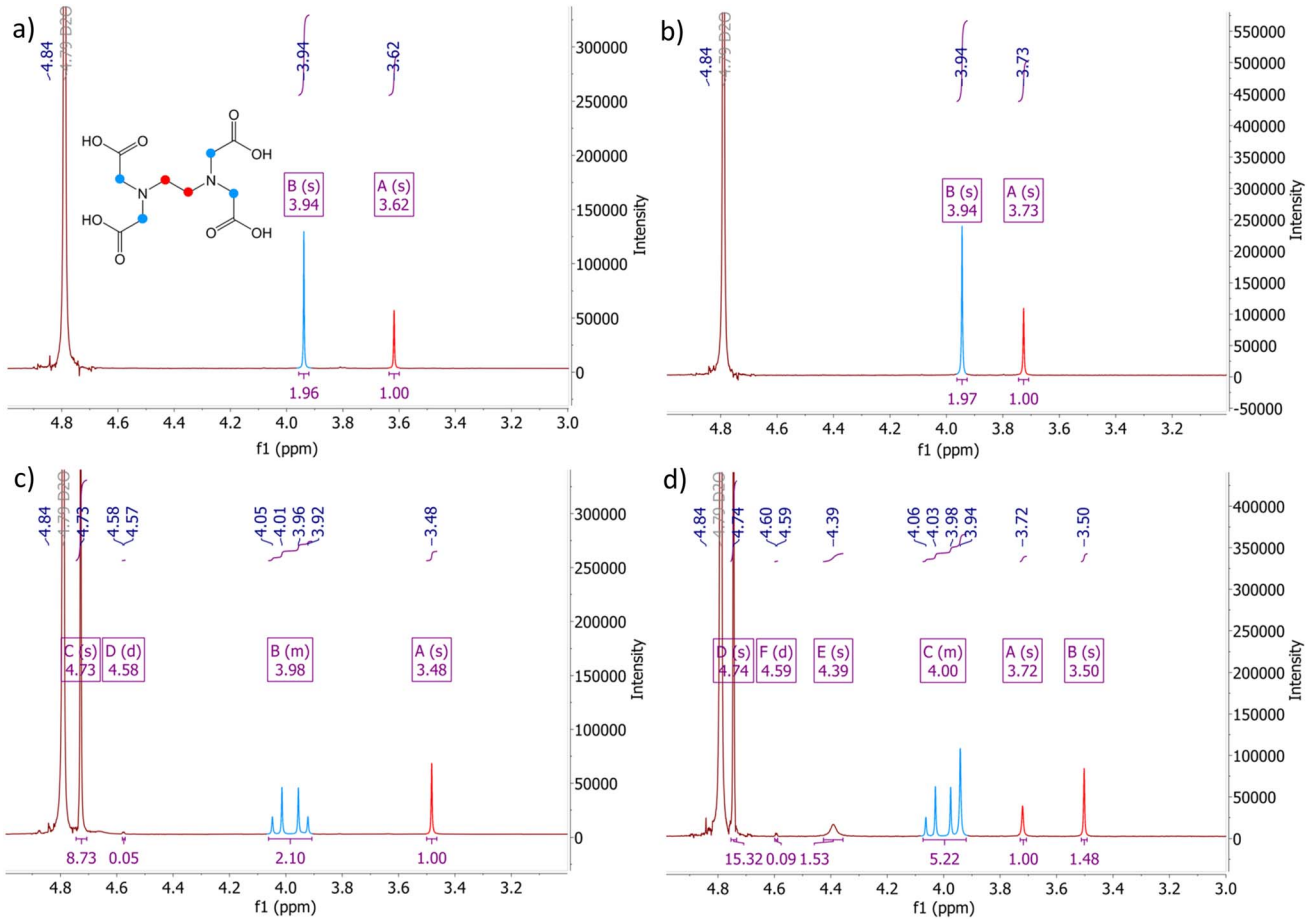

Fig. 3 ^1H NMR spectra of solution containing (a) EDTA in D_2O, showing relative assignments of peaks to groups in EDTA structure, (b) EDTA + STS in D_2O, (c) EDTA + PAT in D_2O and (d) EDTA + STS + PAT in D_2O.

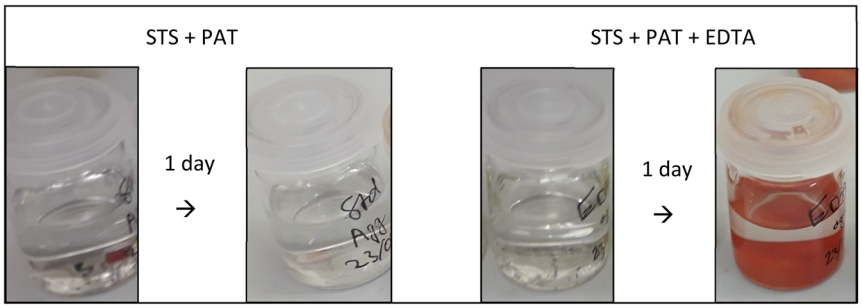

Fig. 4 Vials of STS + PAT and EDTA + STS + PAT in water, showing that upon addition of EDTA, a red powder forms over time in ambient conditions.

splits into an A–B quartet, which is indicative of EDTA complexation.[32] When STS is added to EDTA in D_2O, the backbone CH_2 signal shifts slightly downfield to 3.73 ppm, potentially indicating an interaction between EDTA and STS. The final solution with EDTA, STS and PAT shows both spectra overlapped, indicating that there is likely an STS interaction, as otherwise we would have expected a similar spectrum to EDTA + PAT (without overlap). In the solution with both precursors and EDTA, a broad peak also appears at 4.39 ppm, which indicates an exchangeable H somewhere in the mixture.[33] These results show that there is clearly interaction between PAT and EDTA in solution, but there is also an interaction between STS and EDTA which was previously not identified. It is also still unproven that EDTA is binding specifically to Sb^{3+}. However, due to the high O affinity of Sb, it is most likely the case.[34]

The formation of antimony chalcogenide aggregate in the precursor solution was investigated by mixing two solutions: one with the precursors STS and PAT in water, and another with STS, PAT and EDTA. All reagents were used at the same concentrations used in cell fabrication. Both solutions were left in ambient conditions, and the results are shown in Fig. 4. Initially, both solutions are clear and colourless, however over the course of a few minutes the EDTA-containing solution started to turn orange and opaque. Eventually, the solution once again became clear as the powder, now a deep red, settled to the bottom of the vial.

As presented in Section 2.4 below, we were able to prove that this powder is Sb_2S_3, indicating the direct opposite effect to the suppression of particle aggregation proposed by Wang *et al.*,[17] as EDTA instead *promoted* the formation of these nanoparticles. Although this result was unexpected, we hypothesized that the formation of this red powder, given its correlation with the observed positive effects of EDTA, could potentially serve as a screening method for identifying other promising additives.

2.3 Additive screening process

To perform this screening test, we simply repeated the prior test, placing an additive of an equimolar amount to EDTA into a solution with the two precursors. We tested a series of additives with similar structural moieties to EDTA. The additives tested are listed below in Table 1, along with the colour of the resultant powder. Structures of each additive are shown in Fig. 5, and images of the powders formed are shown in ESI Fig. 5.†

Additives with acid groups generally formed the red powder, while those without formed a white powder. To test the effectiveness of the powder formation as a screening process, cells were fabricated using the additives in Table 1. The champion JV curves and EQE responses are shown in Fig. 6. The cell statistics are shown in ESI Fig. 6 and Table 2.† Significantly, the formation of red powder in the screening process largely correlated with an improvement in performance, while the formation of

Table 1 List of additives tested in screening process and whether or not they formed a red resultant powder (RP) in the aggregation screening process

Additive	Short name	Red RP?
Ethylenediaminetetraacetic acid	EDTA	Yes
Nitrilotriacetic acid	NTA	Yes
Pentetic acid	PA	Yes
Triethylenetetramine-*N*,*N*,*N*′,*N*″,*N*‴,*N*‴-hexaacetic acid	TETAH	Yes
L-(+)-Tartaric acid	LTA	Yes
Diglycolic acid	DGA	Yes
Nitrilotris (methylenephosphonic) acid	NTMP	Yes
1,1′,1″,1‴-(Ethane-1,2-diylbis(azanetriyl))tetrakis (propan-2ol)	1111E	No
Triethanolamine	TEA	No
Ethylenediamine	ED	No
Phosphonic acid	PHA	Yes
Acetic acid	AA	Yes
Hydrochloric acid	HCl	Yes

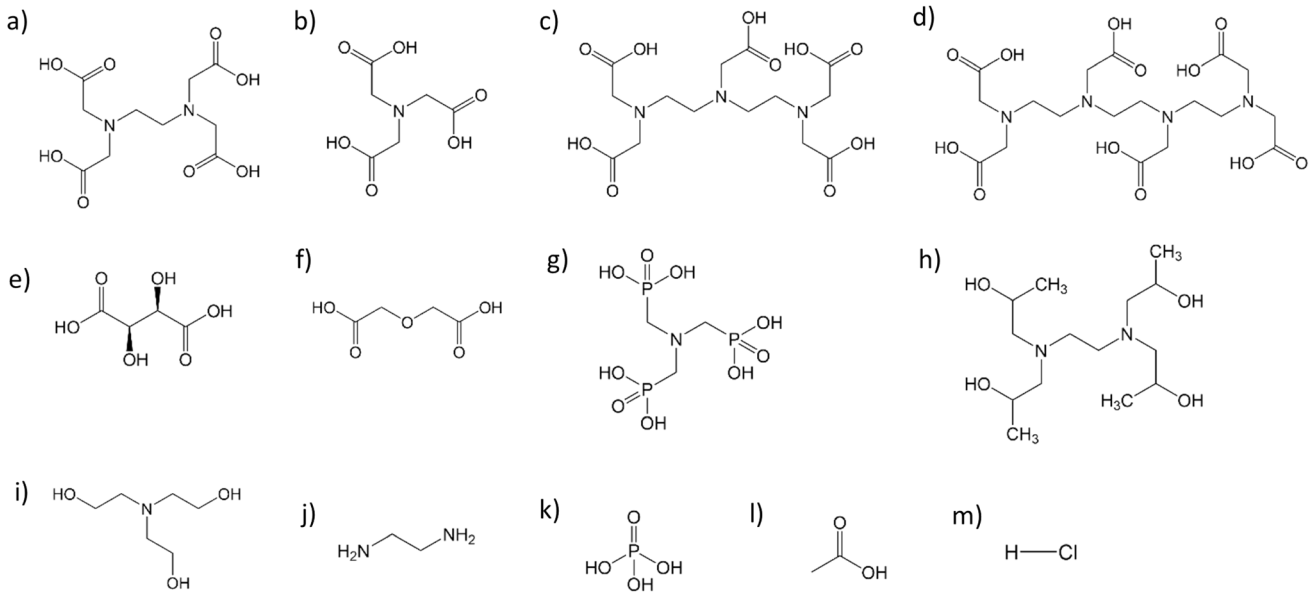

Fig. 5 Chemical structures of additives (a) EDTA, (b) NTA, (c) PA, (d) TETAH, (e) LTA, (f) DGA, (g) NTMP, (h) 1111E, (i) TEA, (j) ED, (k) PHA, (l) AA, and (m) HCl from Table 1.

the white powder correlated with a decrease in performance. In each of the 'red powder' cells, the films looked visually smoother and shiner than the standard (additive-free) and 'white powder' cells. An example of this effect is shown in ESI Fig. 7.† The best three performing additives, pentetic acid (PA), triethylenetetramine-*N*,*N*,*N*′,*N*″,*N*‴,*N*‴-hexaacetic acid (TETAH) and diglycolic acid (DGA) all outperformed EDTA.

To investigate the effects on the film quality further, p-XRD was performed on a selection of films (ESI Fig. 8†), utilising red and white powder forming additives. The effects initially observed with the use of EDTA, specifically (1) a notable increase in the favorable (211) and (221) reflections, and (2) the suppression of Sb_2O_3, were also seen with each of the red-powder-forming additives tested.

SEM-EDS was used to compare the elemental composition and surface morphology of each of the standard, EDTA and high-performing PA films. The EDS results are shown in ESI Table 1.† The Sb : S ratios of the annealed standard, EDTA and PA films were 2 : 2.09, 2 : 2.53, and 2 : 2.55, respectively. This suggests a higher level of incorporation of S into the film for EDTA and PA, indicating that the standard had either sulfur vacancies which would have acted as recombination centres, or the presence of Sb_2O_3 within the film itself, which would have a similar effect. The measured area of the standard was away from the surface Sb_2O_3 formations, and so was, to the best of

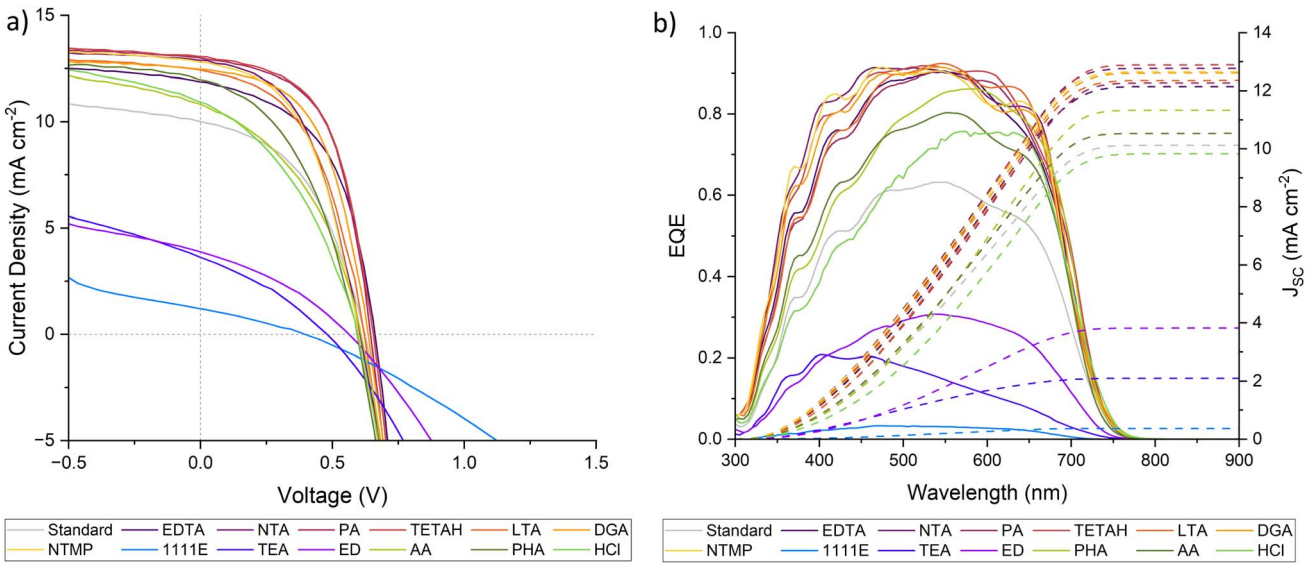

Fig. 6 (a) *J*–*V* curves, and (b) EQE response of champion Sb_2S_3 solar cells with no additive (standard) and with additives listed in Table 1.

our knowledge, representative of the underlying film and not the surface formations.

2.4 Mechanistic understanding of additives

To confirm the identity of the red and white powders, we investigated them using p-XRD and Raman spectroscopy (shown in Fig. 7). We also tested the EDTA and PA powders in SEM-EDS (results in ESI Table 1†). To attain the powders for testing, the solution was decanted. The powder was washed and decanted twice with DI water to remove residual dissolved precursors, then allowed to dry over 24 hours. Upon annealing in the same conditions as the films (350 °C, N_2 atmosphere, 10 min), the red powders turned black. The black powder of the EDTA sample was measured using p-XRD and shown to be crystalline Sb_2S_3 (ESI Fig. 9†), indicating that the red powder was amorphous Sb_2S_3. p-XRD of the unannealed red powder showed no distinct peaks, further indicating an amorphous nature. Raman spectroscopy was a good match for the 'as-deposited', or amorphous Sb_2S_3 of Dielegros-Godines *et al.*,[35] and SEM-EDS results confirmed the composition was a majority of Sb and S, in the Sb : S ratio of 2 : 2.60. These two elements accounted for 93% of the composition, with the remaining 7% comprising C, O, N and Na. These additional components were assumed to be trapped remnants of the precursors and/or EDTA which did not fully wash away. For the white powder, the patterns directly matched literature spectra for cubic Sb_2O_3 in both p-XRD (ICSD collection code 240206) and Raman spectroscopy.[36]

After confirming the identity of the red powder as amorphous Sb_2S_3, we proposed a potential mechanism for the suppression of Sb_2O_3 by the red powder forming additives. The proposed mechanism is as follows.

Release of reactive sulfur species H_2S from STS:[37]

$$S_2O_3^{2-} + 2H^+ \rightleftharpoons H_2S + SO_3 \quad (1)$$

Hydrolysis of Sb_2O_3:[20]

$$Sb_2O_3 + H_2O + 2H^+ \rightleftharpoons 2Sb(OH)_2^+ \quad (2)$$

These can be combined to lead to the formation of Sb_2S_3:

$$2Sb(OH)_2^+ + 3H_2S \rightarrow Sb_2S_3 + 4H_2O + 2H^+ \quad (3)$$

Sb_2O_3 is a known decomposition product of PAT.[38] The decomposition of $S_2O_3^{2-}$ (eqn (1)), the hydrolysis of Sb_2O_3 (eqn (2)) and hence the final formation of Sb_2S_3 (eqn (3)) rely on the presence of H^+, so we considered the effect of pH on the reaction. For each of the eqn (1)–(3), we expected an increase in pH as it occurred due to the consumption of H^+. We prepared relevant solutions to test this hypothesis, and chose to use PA as our acid as it dissolved more readily at room temperature than EDTA, while still giving high efficiency in solar cells. A solution of STS + PA (eqn (1)) showed the expected behaviour by the pH increasing from 3.9 to 4.3 over one day. A solution of PAT + PA became more acidic, changing from 3.9 to 3.7 over the same time period. This was likely due to the release of tartaric acid upon the decomposition of PAT.[25] A solution of STS + PAT + PA (eqn (1)–(3)) yielded the expected result of a larger pH increase, going from 4.2 to 4.7, giving good evidence of the final Sb_2S_3 formation mechanism. Overall, a lower pH allows and promotes this conversion from Sb_2O_3 to Sb_2S_3, as well as the release of sulfur from STS which is known to improve deposition.[19] This understanding aligns with what we see in literature, with the use of acidic additives coinciding with a suppression of Sb_2O_3; for example, Chen *et al.* suppressed Sb_2O_3 formation using a range of acids including phosphotungstic acid,[29] Xiao *et al.* found a reduction in Sb_2O_3 formation when using thioacetamide in conjunction with STS,[19] and Chen *et al.* used Sb_2O_3 as a precursor to Sb_2S_3 by utilising EDTA-2Na and $Al_2(SO_4)_3$.[20] With our proposed mechanisms, the reasons leading to Sb_2O_3

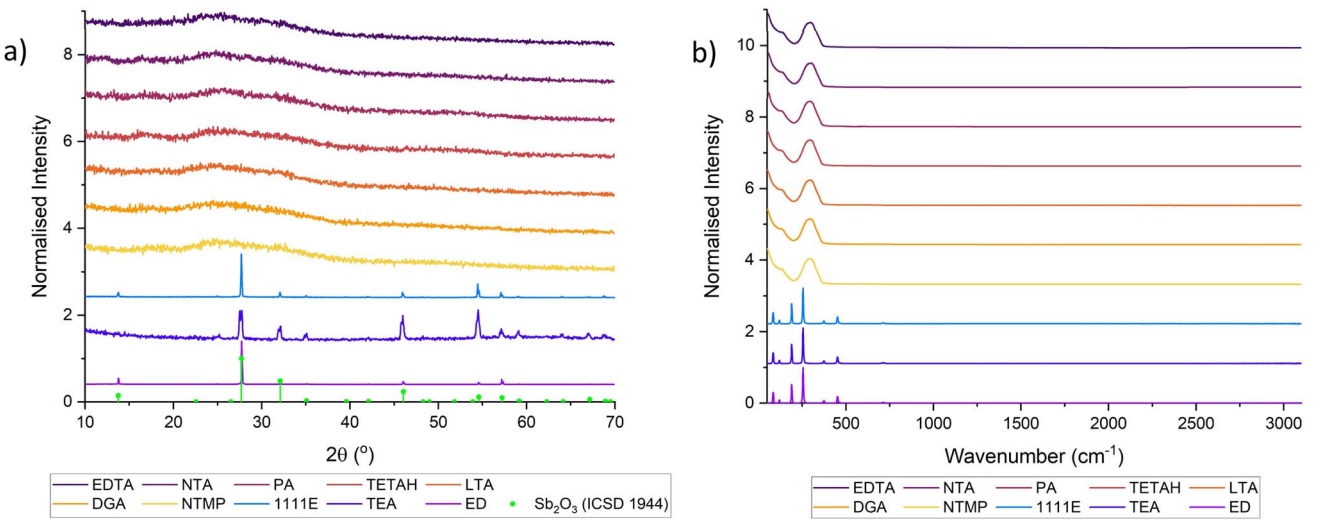

Fig. 7 Results of (a) normalised p-XRD and (b) normalised Raman spectroscopy for red and white powders extracted from screening process solutions. The top 7 spectra in each graph (displayed in red-yellow colours) correspond to red powders (Sb_2S_3), while the bottom three (displayed in blue-purple colours) correspond to white powders (Sb_2O_3).

formation and its suppression, such as was observed in these examples, can be comprehensively understood.

To gain a better understanding of the interaction between white powder additives and precursors, we also measured the NMR of 1111E as a representative additive and compared it with the NMR of EDTA. As shown in ESI Fig. 11,† there was little change to the signals upon the addition of PAT besides some expected chemical shift changes, and a slight increase in a multiplet corresponding to the –OH hydrogens. While this indicated that there may have been some small level of interaction between 1111E and PAT, it was very minor compared to the extent shown by EDTA, which was clearly and completely involved in chelation in the presence of PAT (as evident from the change between Fig. 3a and c where the arm CH_2 signal for EDTA completely converts to an A–B quartet).

We then measured the pH of each additive in water, and correlated that back to the average performance of the cells. The resulting graph is shown in Fig. 8a. Overall, lower pH correlated with the formation of the red powder and higher performance, while a higher pH correlated with the formation of a white powder and lower performance. The standard, with no additive, remained clear and colourless. Fig. 8b shows the correlation of the readiness of an additive to bind with Sb^{3+} (based on available O^- atoms) with the average performance of the additive in Sb_2S_3 solar cells. A general trend can be seen whereby the more available O^- atoms the additive has, the greater its average efficiency. This is in agreement with a recent study by Ren *et al.* in 2025 on the chelation of Sb^{3+} by PO_4^{3-} in $Sb_2(S,Se)_3$ solar cells, whereby the chelation of PO_4^{3-} to Sb^{3+} was evidenced by XPS.[39] There is a noticeable gap between the performance of some of the red-powder forming additives when they are compared relative to their pH, which may be explained by their ability to bind Sb^{3+} and effectively control film deposition. We demonstrated earlier in Fig. 3 that EDTA does bind to something in PAT. Our results correlate performance to this potential chelation ability quite well, as the poorest performing HCl has no sites with Sb affinity, while AA has one carboxylic acid group with 2 O atoms available to bind, PHA has one phosphonic acid group with 3 available O atoms, and so on, until the highest performing PA and TETAH with 5 and 6 carboxylic acid groups, for 10 and 12 available O atoms respectively. Overall, therefore, we agree with Wang *et al.*[17] that EDTA "is able to control the nucleation and deposition process", and this correlation between available 'Sb binding sites' and performance, along with our NMR results which strongly suggest EDTA binds to Sb^{3+}, shown in Fig. 3, and the correlation shown in Fig. 8b, now provide some evidence of these effects.

Among the 10 red powder-forming additives, HCl was an outlier in terms of cell performance. While there were no available Sb^{3+} binding atoms as with the other additives, it actually performed worse than the standard despite suppressing Sb_2O_3 formation. We believe this to be due to an elemental sulfur-forming side reaction caused as a result of very low pH. A detailed explanation of this can be found in the ESI Discussion 2.†

It is worthwhile mentioning that the TEA additive has been previously shown to improve the performance of $Sb_2(S,Se)_3$ solar cells in a study by Zhu *et al.*[40] This appears contradictory to our results; however, they also add HCl, which counteracts the pH effects of TEA observed here, allowing it to perform chelation effects.

In order to investigate the effects of the red Sb_2S_3 aggregate on cell performance (and whether or not a Sb_2S_3 film can still form if the precipitate is removed after forming), we fabricated cells under three conditions; (i) a standard EDTA cell, (ii) a standard EDTA cell, but the mixed precursor solution was left in ambient conditions for a day before hydrothermal synthesis, allowing Sb_2S_3 particles to form and settle out (named 'settled'), and (iii) where a 'settled' solution was prepared, but the particles were then filtered out to leave a clear solution (named

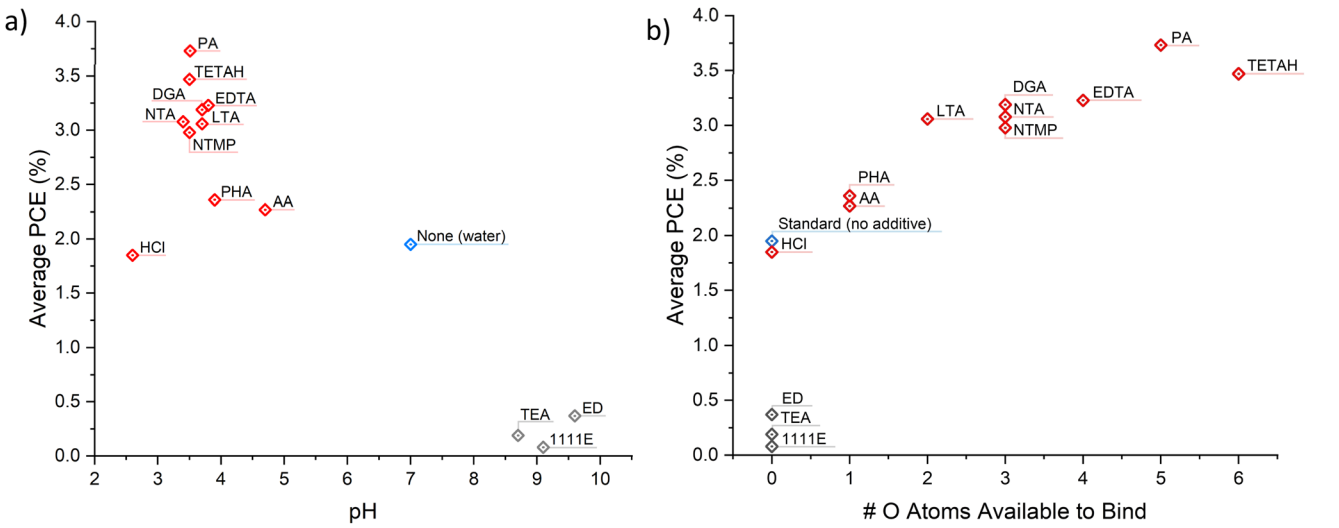

Fig. 8 (a) pH of additives in Table 1 *vs.* average cell performance of Sb_2S_3 solar cells made using that additive, (b) number of O atoms available in each additive to bind to Sb^{3+} *vs.* average Sb_2S_3 solar cell performance. O atoms are considered 'available to bind' if they are readily deprotonated to give O^-, therefore –COOH would count as one available O atom.

'filtered'). The results are shown in detail in ESI Fig. 10.† We observed that for the settled sample, the performance was very similar to the EDTA standard, suggesting that the presence of the Sb_2S_3 powder had little effect on performance. However, once filtered, the performance increased, primarily due to an increase in fill factor, suggesting that the removal of the red Sb_2S_3 aggregate not only still allows a film to form, but actually improves the resultant solar cell's performance.

The fact that the performance is unhindered, and even improved, by allowing the aggregation to occur suggests that the formation of the Sb_2S_3 aggregate does not drastically impact the availability of Sb for film deposition. We propose, therefore, that the Sb_2S_3 aggregate forms as a result of the conversion mechanism from Sb_2O_3, detailed in eqn (1)–(3). By allowing this conversion to occur and removing the particulates afterwards, the 'particle-based' deposition regime (whereby whole nanoparticles deposit onto the film) may be disfavoured over the 'ion-based' deposition regime (whereby individual ions, such as Sb^{3+} bound to EDTA) for film deposition. The ion-based deposition is preferred for larger and more compact grains, which could explain the slight performance gain for the filtered sample.[17]

3 Conclusions

Overall, we have elucidated the working mechanism of the established additive EDTA, leveraging this knowledge to develop a novel screening process for identifying effective additives and understanding their role in Sb_2S_3 solar cells. A simple test involving the addition of an additive to a PAT/STS precursor mixture in water provides direct insight into its effects: the formation of a red Sb_2S_3 precipitate indicates sufficient acidity to convert Sb_2O_3 to Sb_2S_3, while additional colour changes or precipitates signal potential side reactions that may hinder performance. This method offers a straightforward approach for screening additives and detecting unwanted interactions.

Furthermore, we found that additives with a high number of oxygen atoms available for Sb^{3+} chelation performed better, supporting a two-fold working mechanism: (1) pH control—low enough to facilitate sulfur ion release and Sb_2O_3 conversion but not so low as to trigger elemental sulfur formation, and (2) Sb^{3+} chelation, which enhances film deposition. Our findings underscore the critical role of pH regulation in antimony chalcogenide solar cells, demonstrating that high pH promotes Sb_2O_3 formation while low pH drives its conversion to Sb_2S_3. The insights gained from this study not only inform the selection of future additives but also contribute to optimizing the deposition environment for efficient, lightweight solar power applications.

4 Methods

4.1 Reagents

Ethylenediaminetetraacetic acid (EDTA) was acquired from Apex Bio. Phosphonic acid (PHA) was acquired from Fluka Honeywell. Triethanolamine (TEA) and pentetic acid (PA) were acquired from Fluorochem. Triethylenetetramine-*N*,*N*,*N*′,*N*″,*N*‴,*N*‴-hexaacetic acid (TETAH) and sodium thiosulfate (STS) were acquired from Thermo Scientific. Thiourea was acquired from VWR Chemicals. All other reagents were acquired from Merck.

4.2 Fabrication of Sb_2S_3/TiO_2 film

To pattern the bottom FTO electrode, the FTO-coated glass was etched using Zn metal and HCl, then sonicated in Hellmanex in UP water (2%), UP water and ethanol. TiO_2 precursor solution was spin coated onto the substrate, which was masked with polyimide tape: Ti(IV) isopropoxide (140 μL), EtOH (1.984 mL), HCl in EtOH (41.6 μL, 1.25 M); 100 μL at 1650 rpm for 40 seconds. The substrates were annealed (550 °C, 2 °C min^{-1} ramp, hold for 50 min) to yield the TiO_2 film. A seed layer of Sb_2S_3 was deposited in a nitrogen-filled glovebox by spin coating: thiourea (0.1 g), antimony acetate (0.2 g) in 252 μL DMSO/H_2O solution (0.8 : 0.03 v/v), DMSO was added dropwise (1680 μL); coated 100 μL at 4000 rpm for 40 s. This was followed by annealing at 200 °C for 1 minute in the glovebox. The seeded films were placed into 50 mL autoclaves. Hydrothermal solutions were made up by dissolving the additive being used (7.5×10^{-5} moles) in a potassium antimony tartrate hydrate (PAT) solution (15 mL, 19 mM). This solution was then mixed with a sodium thiosulfate (STS) solution (15 mL, 220 mM) and loaded into the autoclave with the film. The autoclaves were placed into a preheated oven at 100 °C for 2 hours, and allowed to cool overnight. The films were washed in UP water, the glass side was wiped clean, and it was dried with nitrogen flow. The films were annealed in the glovebox at 350 °C for 10 minutes to yield the finished film.

4.3 Device assembly

The completed Sb_2S_3/TiO_2 film, still in the glovebox, had a Spiro-OMeTAD solution spin coated: chlorobenzene (1 mL), *tert*-butylpyridine (28.814 μL), LiTFSI solution (9.5 μL, 520 mg mL^{-1} in MeCN) and Spiro-OMeTAD (36.6 mg, Solarpur SHT-263); 100 μL, 3000 rpm, 30 s. The film was heated at 100 °C for 10 minutes in air to dope Spiro-OMeTAD. The edges of the cell were etched using acetonitrile, then a KOH (5 M) solution. The etched cells were loaded into a thermal evaporator and the gold electrodes were deposited (5×10^{-6} mbar, 80 nm@0.5 Å s^{-1}).

4.4 Aggregation screening test

The additive (1.25×10^{-5} moles) was dissolved in PAT solution (2.5 mL, 38 mM) in ultrapure water. If the additive did not fully dissolve, it was swirled vigorously for a few minutes. A STS solution (2.5 mL, 440 mM) in ultrapure water was then added and the solution was swirled to yield a homogenous solution. This solution was left in a vial to react and settle over the course of one week.

The aggregate was collected by decanting the water when settled, then refilling with fresh ultrapure water, sonicating and shaking through to remove unreacted PAT and STS. This process was repeated again once the powder had settled, and the final liquid was decanted once settled again. The resulting

wet powder was allowed to dry overnight to yield the final product.

4.5 Materials characterisation

Crystalline information was collected on a Bruker D2 Phaser benchtop powder X-ray (p-XRD) diffractometer with Cu Kα radiation ($\lambda = 1.54184$ Å).

SEM (4 nm Pd coating, WD = 7 mm, 10 kV) was used to attain morphological data, while SEM-EDS was used for elemental analysis of the films. EDS data was collected and processed using Oxford Instruments AZtec software.

Raman spectroscopy was performed at 785 nm with laser power of 0.2 mW.

NMR spectra were collected on a Bruker Avance spectrometer δ_H (500 MHz; D_2O; Me_4Si).

pH testing was performed using a Hanna Instruments HI98103 pH tester, calibrated against a HI70007P 7.01 pH buffer solution. The probe was inserted into the solution to be tested until a stable reading could be taken.

4.6 Solar cell characterisation

The complete solar cells were characterised by JV measurement and EQE. JV measurement was carried out using an AM1.5G solar simulator and a Keithley 2450 sourcemeter to apply bias voltage. The scans were done from −0.5 V to 1.5 V at 0.125 V s^{-1} with a step size of 0.035 V. The active area of the device was 0.04785 cm^2, made using an aluminium mask. EQE measurements were taken using a dual-source quartz halogen and xenon lamp setup (Bentham ILD_75E powered by 2× Bentham 610 power sources with Bentham 418 optical chopper controller and 2-slot chopper blade) which was monochromated (Bentham TMc300 Monochromator), passed through a square 1.5 mm aperture and focussed onto the sample, with a masked active area of 0.04785 cm^2. A reference silicon diode (Bentham DH-Si) with a known responsivity at the same fixed distance was used to calculate the EQE of the device. Data was collected using a Stanford Research Systems Model SR830 DSP lock-in amplifier connected to the cell.

Data availability

The data supporting this article have been included as part of the ESI.†

Conflicts of interest

There are no conflicts to declare.

Acknowledgements

T. A. acknowledges finance support of DFG Heisenberg Programme, project AM 519/4-1. We acknowledge P. Valluri (University of Edinburgh) for additional supervision provided for M. S. during his PhD studies. We thank University of Edinburgh technicians G. Steedman and L. Mitchell for their assistance with equipment setup and maintenance, R. York and J. Bella for help with NMR measurements, G. Nichol for help with XRD measurements, A. Gromov for help with Raman measurements, and N. Cayzer for help with SEM/EDS measurements.

References

1 *Statistical Review of World Energy*, Energy Institute, **https://www.energyinst.org/statistical-review**, 2024.
2 *Energy Production and Consumption*, Global Data Change Lab, **https://ourworldindata.org/energy-production-consumption**, 2020.
3 C. Jiang, J. Zhou, R. Tang, W. Lian, X. Wang, X. Lei, H. Zeng, C. Zhu, W. Tang and T. Chen, *Energy Environ. Sci.*, 2021, **14**, 359–364.
4 R. Tang, X. Wang, W. Lian, J. Huang, Q. Wei, M. Huang, Y. Yin, C. Jiang, S. Yang, G. Xing, S. Chen, C. Zhu, X. Hao, M. A. Green and T. Chen, *Nat. Energy*, 2020, **5**, 587–595.
5 Y. Yin, C. Jiang, Y. Ma, R. Tang, X. Wang, L. Zhang, Z. Li, C. Zhu and T. Chen, *Adv. Mater.*, 2021, **33**, 2006689.
6 C. Wu, W. Lian, L. Zhang, H. Ding, C. Jiang, Y. Ma, W. Han, Y. Li, J. Zhu, T. Chen and C. Zhu, *Sol. RRL*, 2020, **4**, 1900582.
7 C. Wu, C. Jiang, X. Wang, H. Ding, H. Ju, L. Zhang, T. Chen and C. Zhu, *ACS Appl. Mater. Interfaces*, 2019, **11**, 3207–3213.
8 L. Wang, D.-B. Li, K. Li, C. Chen, H.-X. Deng, L. Gao, Y. Zhao, F. Jiang, L. Li, F. Huang, Y. He, H. Song, G. Niu and J. Tang, *Nat. Energy*, 2017, **2**, 17046.
9 M. M. Nicolás-Marín, F. Ayala-Mato, O. Vigil-Galán and M. Courel, *Sol. Energy*, 2021, **224**, 245–252.
10 Y. Pan, X. Hu, Y. Guo, X. Pan, F. Zhao, G. Weng, J. Tao, C. Zhao, J. Jiang, S. Chen, P. Yang and J. Chu, *Adv. Funct. Mater.*, 2021, **31**, 2101476.
11 C. Wu, L. Zhang, H. Ding, H. Ju, X. Jin, X. Wang, C. Zhu and T. Chen, *Sol. Energy Mater. Sol. Cells*, 2018, **183**, 52–58.
12 S. Fan, C. Shi, K. Lv, Q. Wang, F. Guo and W. Chen, *J. Nanopart. Res.*, 2021, **23**, 42.
13 L. Zhang, W. Lian, X. Zhao, Y. Yin, T. Chen and C. Zhu, *ACS Appl. Energy Mater.*, 2020, **3**, 12417–12422.
14 W. Han, D. Gao, R. Tang, Y. Ma, C. Jiang, G. Li, T. Chen and C. Zhu, *Sol. RRL*, 2021, **5**, 2000750.
15 Z. Li, X. Liang, G. Li, H. Liu, H. Zhang, J. Guo, J. Chen, K. Shen, X. San, W. Yu, R. E. I. Schropp and Y. Mai, *Nat. Commun.*, 2019, **10**, 125.
16 X. Jin, Y. Fang, T. Salim, M. Feng, S. Hadke, S. W. Leow, T. C. Sum and L. H. Wong, *Adv. Funct. Mater.*, 2020, **30**, 2002887.
17 X. Wang, R. Tang, C. Jiang, W. Lian, H. Ju, G. Jiang, Z. Li, C. Zhu and T. Chen, *Adv. Energy Mater.*, 2020, **10**, 2002341.
18 Y. Zhao, S. Wang, C. Jiang, C. Li, P. Xiao, R. Tang, J. Gong, G. Chen, T. Chen, J. Li and X. Xiao, *Adv. Energy Mater.*, 2022, **12**, 2103015.
19 S. Wang, Y. Zhao, B. Che, C. Li, X. Chen, R. Tang, J. Gong, X. Wang, G. Chen, T. Chen, J. Li and X. Xiao, *Adv. Mater.*, 2022, **34**, 2206242.
20 L. Zhang, P. Xiao, B. Che, J. Yang, Z. Cai, H. Wang, J. Gao, W. Liang, C. Wu and T. Chen, *ChemSusChem*, 2023, **16**, e202202049.

21 Y. Huang, R. Tang, P. Xiao, B. Che, Y. Wang, H. Gao, G. Wang, C. Zhu and T. Chen, *ACS Appl. Mater. Interfaces*, 2022, **14**, 54822–54829.
22 X. Chen, B. Che, Y. Zhao, S. Wang, H. Li, J. Gong, G. Chen, T. Chen, X. Xiao and J. Li, *Adv. Energy Mater.*, 2023, **13**, 2300391.
23 G.-Y. Chen, W.-X. Zhang and A.-W. Xu, *Mater. Chem. Phys.*, 2010, **123**, 236–240.
24 R. Nie and S. I. Seok, *Small Methods*, 2020, **4**, 1900698.
25 Y. Huang, R. Tang, G. Wang, G. Li, B. Che, Y. Wang, W. Lian, C. Zhu and T. Chen, *J. Mater. Chem. A*, 2022, **10**, 9892–9901.
26 P. Kowalczewski and L. C. Andreani, *Sol. Energy Mater. Sol. Cells*, 2015, **143**, 260–268.
27 S. Chen, M. Li, Y. Zhu, X. Cai, F. Xiao, T. Ma, J. Yang, G. Shen, A. Ke, Y. Lu, W. Liang, H.-Y. Hsu, C. Chen, J. Tang and H. Song, *Adv. Energy Mater.*, 2022, **12**, 2202897.
28 B. Che, Z. Cai, H. Xu, S. Sheng, Q. Zhao, P. Xiao, J. Yang, C. Zhu, X. Zheng, R. Tang and T. Chen, *Angew. Chem., Int. Ed.*, 2025, e202425639.
29 Y. Zhang, S. a. Li, R. Tang, X. Wang, C. Chen, W. Lian, C. Zhu and T. Chen, *Energy Technol.*, 2018, **6**, 2126–2131.
30 Y. C. Choi, D. U. Lee, J. H. Noh, E. K. Kim and S. I. Seok, *Adv. Funct. Mater.*, 2014, **24**, 3587–3592.
31 E. Mathuthu, A. Janse van Rensburg, D. Du Plessis and S. Mason, *Biochem. Cell Biol.*, 2021, **99**, 465–475.
32 E. Hafer, U. Holzgrabe, K. Kraus, K. Adams, J. M. Hook and B. Diehl, *Magn. Reson. Chem.*, 2020, **58**, 653–665.
33 P. Charisiadis, V. G. Kontogianni, C. G. Tsiafoulis, A. G. Tzakos, M. Siskos and I. P. Gerothanassis, *Molecules*, 2014, **19**, 13643–13682.
34 R. S. Multani, T. Feldmann and G. P. Demopoulos, *Hydrometallurgy*, 2016, **164**, 141–153.
35 C. Diliegros Godines, J. Santos, N. Mathews and M. Pal, *J. Mater. Sci.*, 2018, **53**, 11562–11573.
36 Z. Sui, S. Hu, H. Chen, C. Gao, H. Su, A. Rahman, R. Dai, Z. Wang, X. Zheng and Z. Zhang, *J. Mater. Chem. C*, 2017, **5**, 5451–5457.
37 W. A. Pryor, *J. Am. Chem. Soc.*, 1960, **82**, 4794–4797.
38 J. R. Reddy, G. Ravi, P. Suresh, N. K. Veldurthi, R. Velchuri and M. Vithal, *J. Therm. Anal. Calorim.*, 2014, **115**, 1321–1327.
39 D. Ren, B. Fu, J. Xiong, Y. Wang, B. Zhu, S. Chen, Z. Li, H. Ma, X. Zhang, D. Pan, B. Zou and G. Liang, *Adv. Mater.*, 2025, **37**, 2416885.
40 Q. Zhu, W. Wang, Z. Chen, Z. Cao, W. Wang, X. Feng, H. Deng, C. Zhang, Q. Zheng, J. Wu, Y. Zhang and S. Cheng, *Small*, 2025, **21**, 2408978.